Supporting Information

Concave Surface-Enriched Reactant Boosts Electrocatalytic C_2H_4 Production from Coal-Derived C_2H_2 via π-Electron Delocalization Effect

Li Li et al.

1. Experimental section.

1.1 Chemicals.

Copper nitrate ($Cu(NO_3)_2 \cdot 3H_2O$, 99.0%), N,N-dimethylformamide (DMF), polyvinyl pyrrolidone (PVP, M_w=15000-19000), tannic acid (TA, 99.0%), anhydrous ethanol (CH_3CH_2OH, 99.9%), and 1,3,5-benzene tricarboxylic acid (H_3BTC) were purchased from Aladdin Ltd. (Shanghai, China). The simulated raw coal-derived C_2H_2 with concentrations of ~15% and 3% H_2/Ar were purchased from Lian Bo (Tianjin, China) Co., Ltd. Deionized water (DIW) was used in all the experimental processes. All the chemicals used were of analytical grade and used without further purification.

1.2 Synthesis of Cu-MOF precursors

According to the previous literature[1], the Cu-MOF precursors were prepared by a PVP-assisted strategy as follows. First, 1.46 g of $Cu(NO_3)_2 \cdot 3H_2O$ and 0.7 g of H_3BTC were dissolved in 20 mL of DMF to form solution A and solution B, respectively. Subsequently, 0.5 g PVP was added to solution A and stirred for 5 min to obtain a homogenous solution. Then, solution B was mixed with solution A and stirred for an additional 10 min. Afterwards, the mixture was transferred to a 100 mL Teflon-lined stainless-steel autoclave and maintained at 80 ℃ for 24 h. Finally, the blue precipitates were harvested by centrifugation, washed with DIW and ethanol several times, and dried in a vacuum oven overnight to produce the Cu-MOF precursors.

1.3. Synthesis of Cu-TA.

The as-prepared Cu-MOF precursors (100 mg) and tannic acid (TA) were first dispersed into 50 mL of DIW to form two solutions. The two solutions were subsequently mixed at room temperature and

stirred for 30 min. Afterwards, the mixture was put into an oil bath at 50 ℃ and refluxed under continuous magnetic stirring (stirring speed: 700 rpm) for 7 h. The precipitate was then washed with DIW and absolute ethanol at least three times to remove the residual TA and dried at 70 ℃ in a vacuum oven overnight.

1.4 Synthesis of Cu-PCC and Cu-C

To obtain Cu-PCC and Cu-C, the as-prepared Cu-TA and Cu-MOF precursors were annealed at 400 ℃ for 2 h at a heating rate of 10 ℃ min^{-1} under a 3% H_2/Ar atmosphere. The mixture was then cooled to room temperature naturally.

2. Electrochemical measurements in the flow cell.

Electrochemical measurements were carried out in a typical flow cell consisting of a GDL as the working electrode, Pt foil as the counter electrode, and Hg/HgO as the reference electrode using a CS150H electrochemical workstation. The cathode cell and anode cell were separated by a Nafion 117 proton exchange membrane. The cathode and anode electrolytes were both composed of 1.0 M KOH solution, and a peristaltic pump was used to circulate the liquid phase. The gas flow rate was controlled by the mass flowmeter. Before the performance tests, the working electrode was fixed at the interface between the gas flow block and the cathodic electrolyte block by conductive copper tape. First, electrochemical semihydrogenation of acetylene was conducted at different applied potentials for 10-20 min to achieve relatively stable and reliable performance parameters before quantitative analysis. The gas at the flow cell outlet was directly introduced into the gas chromatography system for the analysis of the products. All the LSV curves were *iR* compensated

with a compensation level of 70%. For Tafel slopes, the LSV curves were replotted by using the logarithms of the current density as the x-axis and the potential as the y-axis. The obtained slopes of the linear part of the replotted figure were the Tafel slopes.

3. Quantitative analysis of the C_2H_2 conversion, evolution rate, and FE of the obtained products.

The products were subjected to a GC-2010 gas chromatograph equipped with an activated carbon packed column (with He as the carrier gas) and a barrier discharge ionization detector. The C_2H_2 conversion and evolution rate of the different products were calculated using equations (1) and (2), and the FEs of the different products were calculated using equation (3). All the experiments were repeated three times.

$$\text{Conversion (\%)} = \frac{\text{the peak area of B-peak area of A}}{\text{the peak area of B}} \times 100\% \quad (1)$$

$$\text{Evolution Rate (mmol/mg/h)} = \frac{\text{the peak area of X} \times C}{\text{the peak area of standard gas} \times m} \times S \quad (2)$$

$$\text{FE}_X\ (\%) = \frac{\text{a} \times n_X \times F}{Q} \quad (3)$$

X: The different products, including H_2, C_2H_4, and C_2H_6.

C: The concentration of X in standard gas.

m: The mass of metallic Cu over the electrode.

n: The moles of different products, including H_2, C_2H_4, and C_2H_6.

A: Area of the C_2H_2 outlet; B: area of the C_2H_2 inlet.

S: The gas flow rate.

a: The electron transfer number.

F: Faraday constant.

Q: The total Coulomb number of the ESAE process.

4. Electrochemical *in situ* Raman measurements.

In situ electrochemical Raman spectra were recorded via an electrochemical workstation on a Renishaw inVia reflex Raman microscope under 532 nm laser excitation under controlled potentials. We used a homemade Teflon electrolytic cell equipped with a piece of round quartz glass for the incident of lasers and protection of the tested samples. Before the experiments, the electrolyte was pretreated with pure C_2H_2 gas to obtain C_2H_2-saturated KOH. The working electrode was parallel to the quartz glass to maintain the plane of the sample perpendicular to the incident laser. The Pt wire was rolled to a circle around the working electrode to serve as the counter electrode. The reference electrode was Hg/HgO with an internal reference electrolyte of 1.0 M KOH. The spectrum was recorded under applied potentials ranging from 0.2 to −1.0 V vs. RHE.

5. Electrochemical *in situ* ATR-FTIR measurements

In situ ATR-FTIR was performed on a Nicolet 6700 FTIR spectrometer equipped with an MCTA detector with silicon as the prismatic window and an ECIR-II cell by Linglu Instruments. First, Cu-PCC was carefully dropped on the surface of the gold film, which was chemically deposited on the surface of the silicon prismatic material before each experiment. Then, the deposited silicon prismatic material served as the working electrode. Pt foil and Hg/HgO with an internal reference electrolyte of 1.0 M KOH were used as the counter and reference electrodes, respectively. A 1 M KOH solution was used as the electrolyte. The electrolyte was presaturated with pure C_2H_2 gas, and the gas was continuously bubbled through during the whole measurement. The spectrum was

recorded every 30 s under an applied potential ranging from 0.2 to −1.0 V vs. RHE.

6. Electrochemical *operando* online DEMS analysis.

Operando online DEMS analysis was conducted by a QAS 100 instrument provided by Linglu Instruments (Shanghai) Co., Ltd. Because the products in the proposed ESAE process were all in the gas phase, *operando* experiments were conducted to monitor the distribution of the products during the on-stream reaction, clarifying the selectivity issues more directly and clearly. The flow cell used in the performance evaluation and the DEMS were coupled together to ensure that the gas at the flow cell outlet was directly injected into the negatively pressured gas circuit system of the DEMS through a quartz capillary that was inserted into the outlet of the flow cell. The LSV test and rectangular wave current density were applied from 0.2 to −0.8 V vs. RHE with a constant interval of 400 s by means of a CS150H electrochemical workstation. During the experiment, the flow rates of C_2H_2 gas and the electrolyte were set the same as those used for the performance evaluation.

7. General characterizations

Quasi-*in situ* powder X-ray diffraction (XRD) was performed on a Bruker D8 Focus Diffraction System (Germany) using a Cu *K*α radiation source (λ=0.154178 nm). Scanning electron microscopy (SEM) was conducted with an FEI Apreo S LoVac microscope (10 kV). Transmission electron microscopy (TEM) and high-resolution transmission electron microscopy (HRTEM) images were obtained with a JEOL-2100F system equipped with an EDAX Genesis XM2. X-ray photoelectron spectroscopy (XPS) was conducted with a PHI-1600 X-ray photoelectron spectrometer equipped with Al *K*α radiation. All the peaks were calibrated with the Ti 2*p* spectrum since C 1 s is a key

parameter in our research. The Raman spectra were obtained with a Renishaw inVia reflex Raman microscope under an excitation of 514 nm laser with the power of 20 mW. Fourier transform infrared spectroscopy (FTIR) was performed on a Nicolet IS50. The Brunauer–Emmett–Teller (BET) surface area was measured by N2 adsorption using a Micromeritics ASAP 2460

8. DFT calculation.

All the DFT calculations were performed using the Vienna Ab initio Simulation Package (VASP)[2]. The projector augmented wave (PAW) pseudopotential[3] with the PBE generalized gradient approximation (GGA) exchange-correlation function[4] was utilized in the computations. The cutoff energy of the plane wave basis set was 500 eV, and a Monkhorst-Pack mesh of 3×3×1 was used in K-sampling for the adsorption energy calculations and other nonself-consistent calculations. The long-range dispersion interaction was described by the DFT-D3 method. The electrolyte was incorporated implicitly with the Poisson-Boltzmann model implemented in VASPsol[5]. The relative permittivity of the media was chosen as $\epsilon_r = 78.4$, corresponding to that of water. All atoms were fully relaxed with an energy convergence tolerance of 10^{-5} eV per atom, and the final force on each atom was < 0.05 eV $Å^{-1}$.

The transition state (TS) searches were performed using the Dimer method in the VTST package. The final force on each atom was < 0.1 eV $Å^{-1}$. The TS search is conducted by using the climbing-image nudged elastic band (CI-NEB) method to generate initial guess geometries, followed by the dimer method to converge to the saddle points.

The adsorption energy of the reaction intermediates can be computed using Eqs. (1)-(2):

$$\Delta E = E_{*ads} - (E_{*} + E_{ads}) \quad (1)$$

$$\Delta G = \Delta E + \Delta E_{ZPE} - T\Delta S \quad (2)$$

where ΔE_{ZPE} is the zero-point energy change and ΔS is the entropy change. In this work, the values of ΔE_{ZPE} and ΔS were obtained via vibration frequency calculations.

7. Additional Characterization and Results

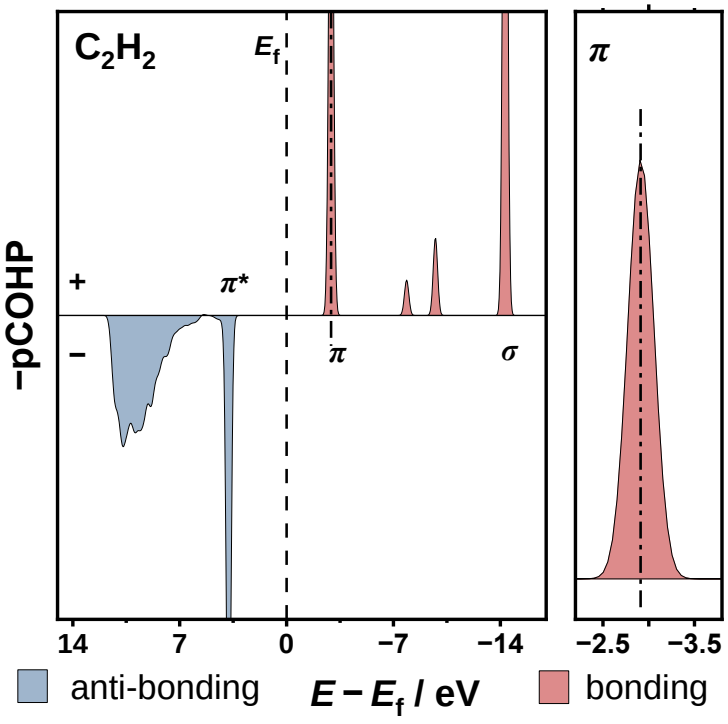

Figure S1. Projected crystal orbital Hamilton population (−pCOHP) for the C-C interaction of gaseous C_2H_2.

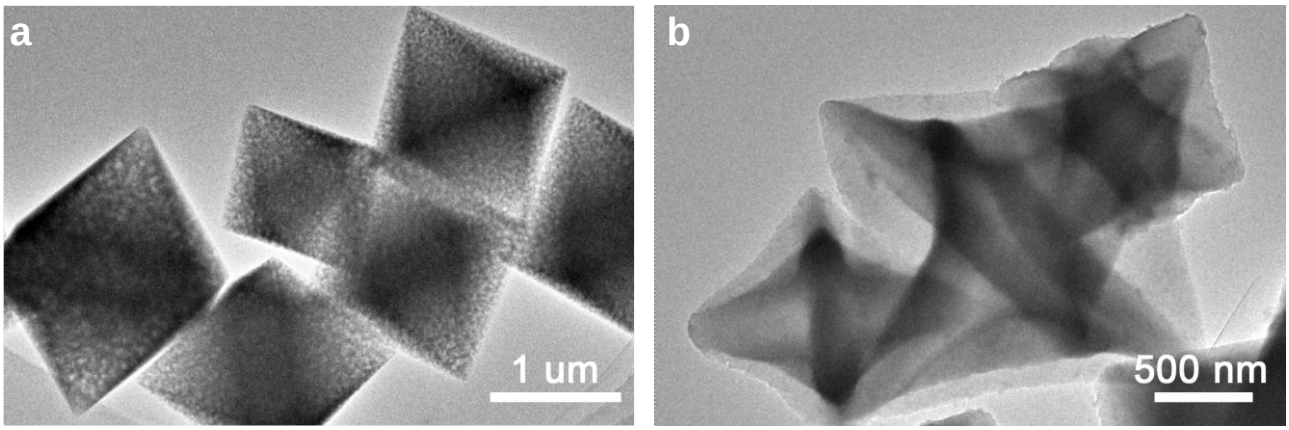

Figure S2. a, b) TEM images of the Cu-MOF precursors (a) and the as-prepared TA-Cu (b).

As shown in the corresponding TEM images, the plate surface of the Cu-MOF precursors collapsed after etching by TA for 7 h due to the Kirkendall effect[6].

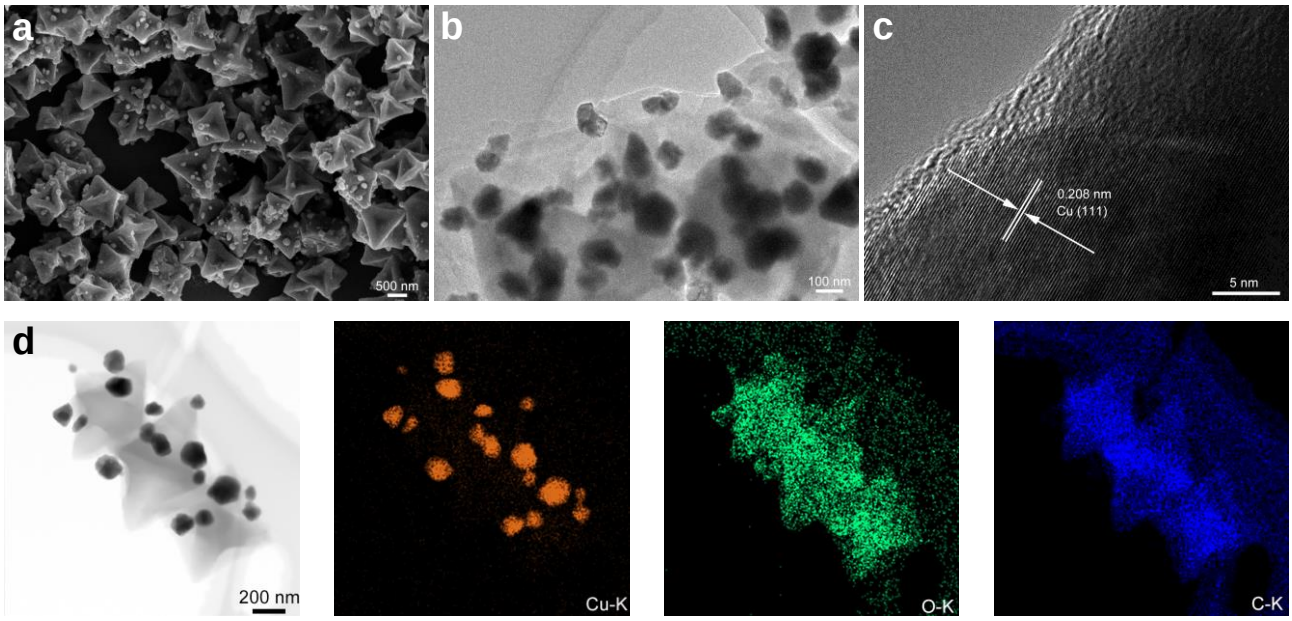

Figure S3. a-c) SEM (a), TEM (b), and HRTEM (c) images of Cu-PCC and the corresponding image of Cu-PCC from scanning transmission electron microscopy under high-angle annular dark-field mode and energy-dispersive X-ray spectroscopy (EDS) elemental mapping images of Cu-PCC (d).

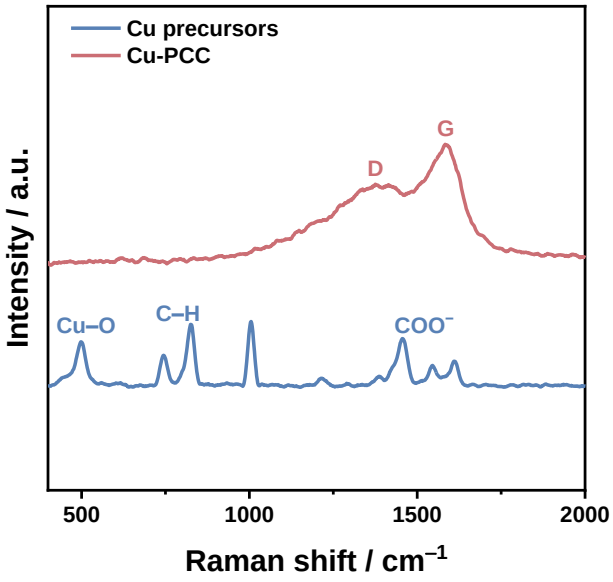

Figure S4. The Raman spectra of the Cu-MOF precursors and the as-prepared Cu-PCC.

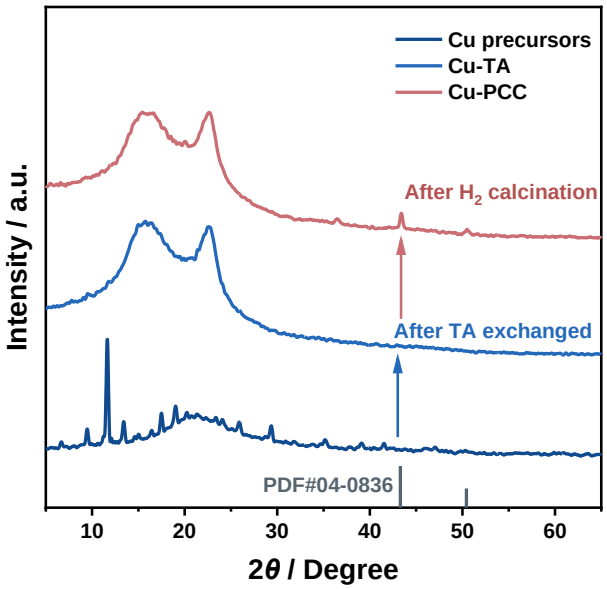

Figure S5. XRD patterns of the Cu-MOF precursors, Cu-TA, and Cu-PCC.

As shown in Figure S5, the crystalline structure of the as-prepared Cu-MOF precursors is similar to that in the reported literature[1,] and these diffraction peaks disappear after the reaction of Cu-MOF precursors with TA due to the amorphous character of the TA-metal complex. Furthermore, diffraction peaks attributed to metallic Cu appear after H_2 calcination, confirming the existence of metallic Cu.

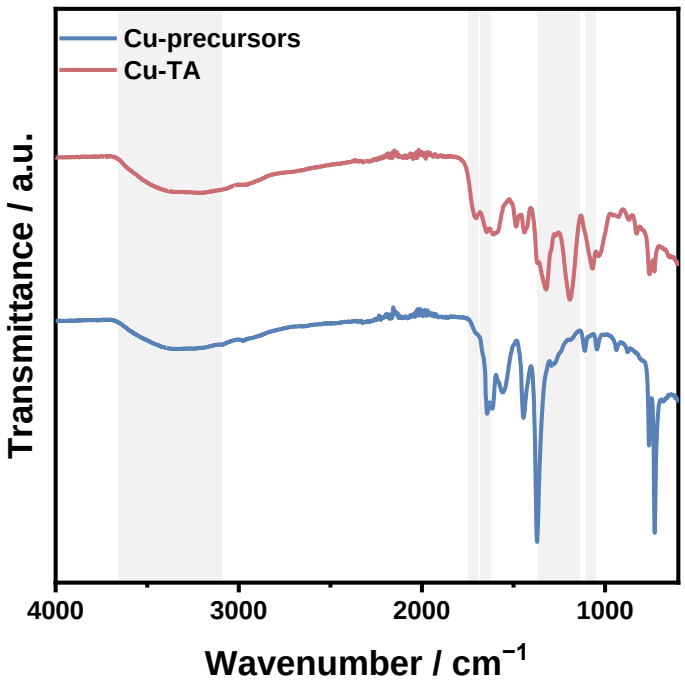

Figure S6. FTIR spectra of Cu-TA and Cu-MOF precursors.

According to the literature,[7–10] the IR data suggest that all the peaks are attributed to the stretching vibration of functional groups from TA, indicating the substitution of H_3BTC by TA and the formation of Cu-TA complexes.

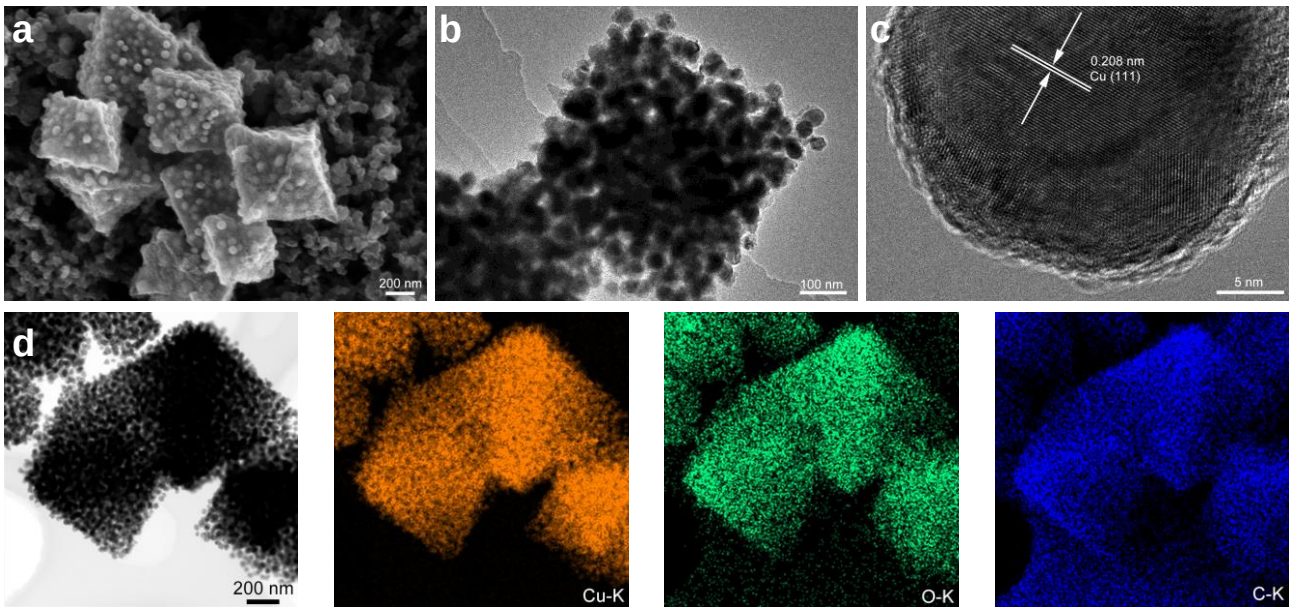

Figure S7. a-c) SEM (a), TEM (b), and HRTEM (c) images of Cu-C and the corresponding image of Cu-C from scanning transmission electron microscopy under high-angle annular dark-field mode and EDS elemental mapping images of Cu-C (d).

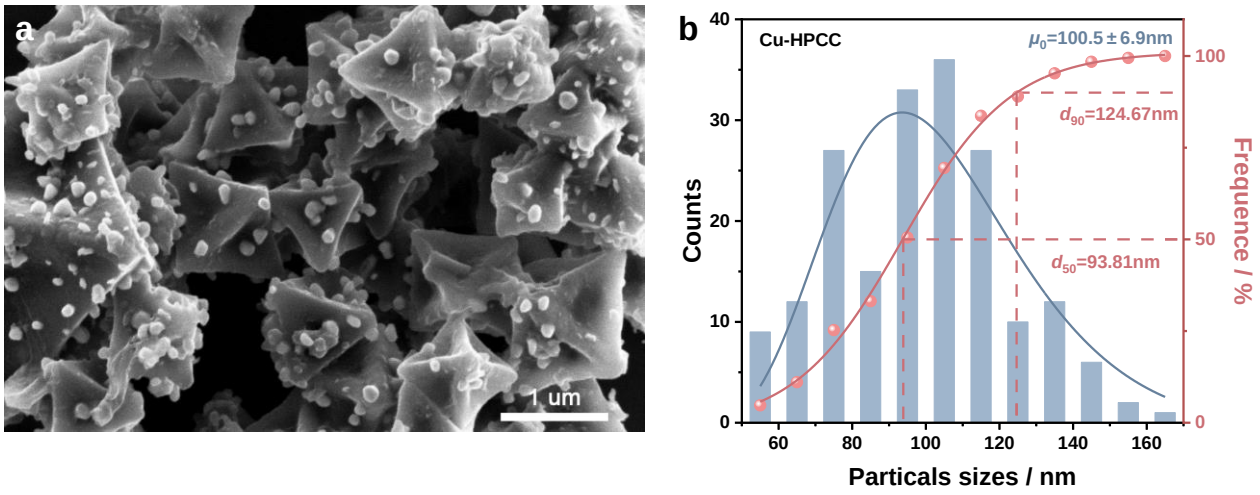

Figure S8. a, b) SEM images of Cu-PCC (a) and the corresponding particle size distribution (b).

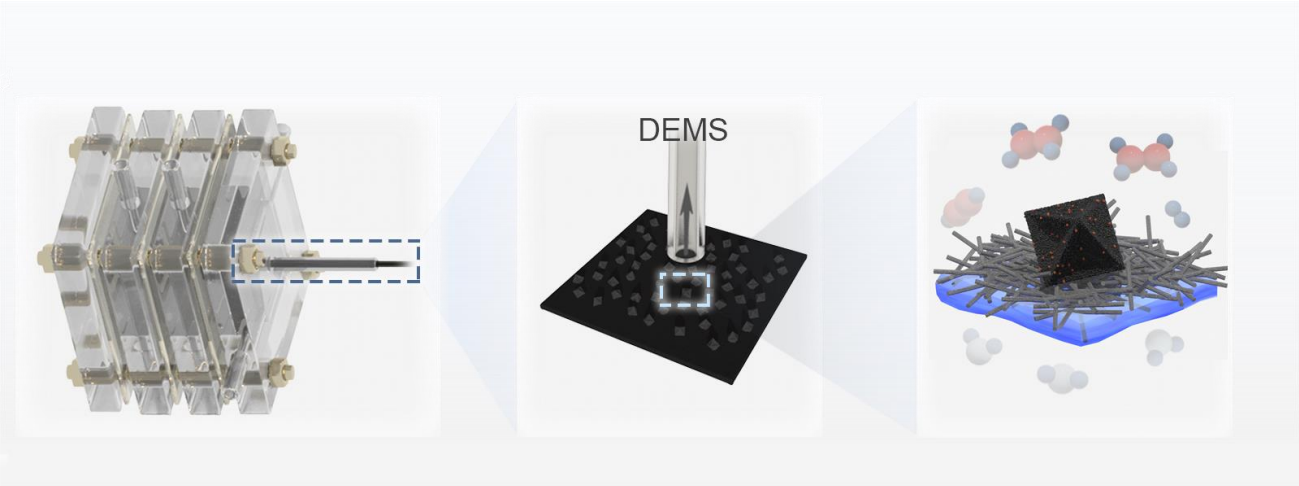

Figure S9. Schematic illustration of the equipment applied in the online *operando* DEMS analysis.

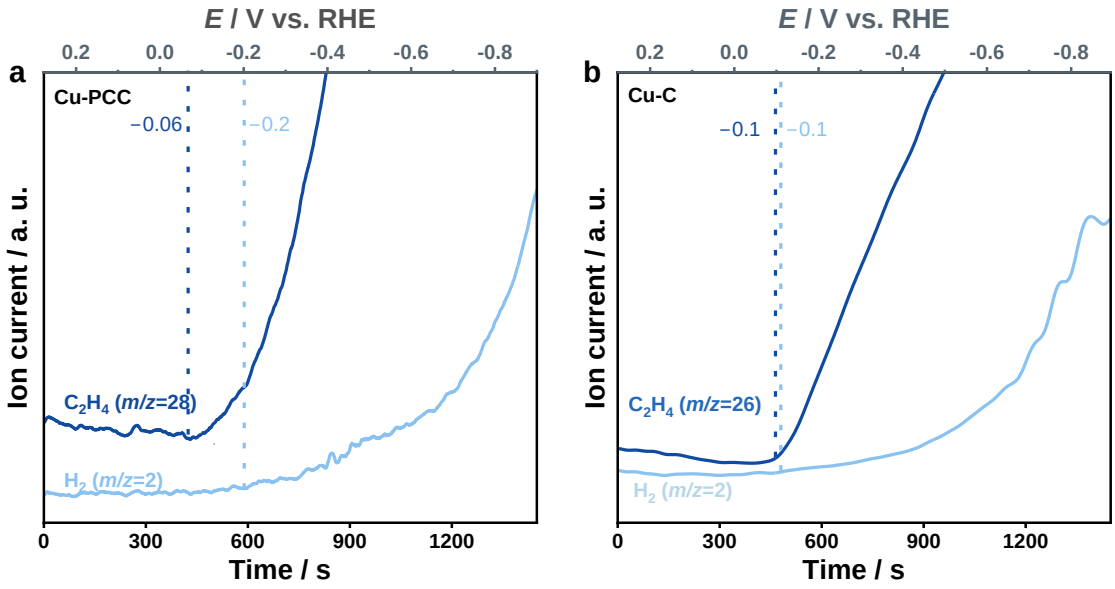

Figure S10. a, b) Enlarged online *operando* DEMS in LSV mode for Cu-PCC and Cu-C.

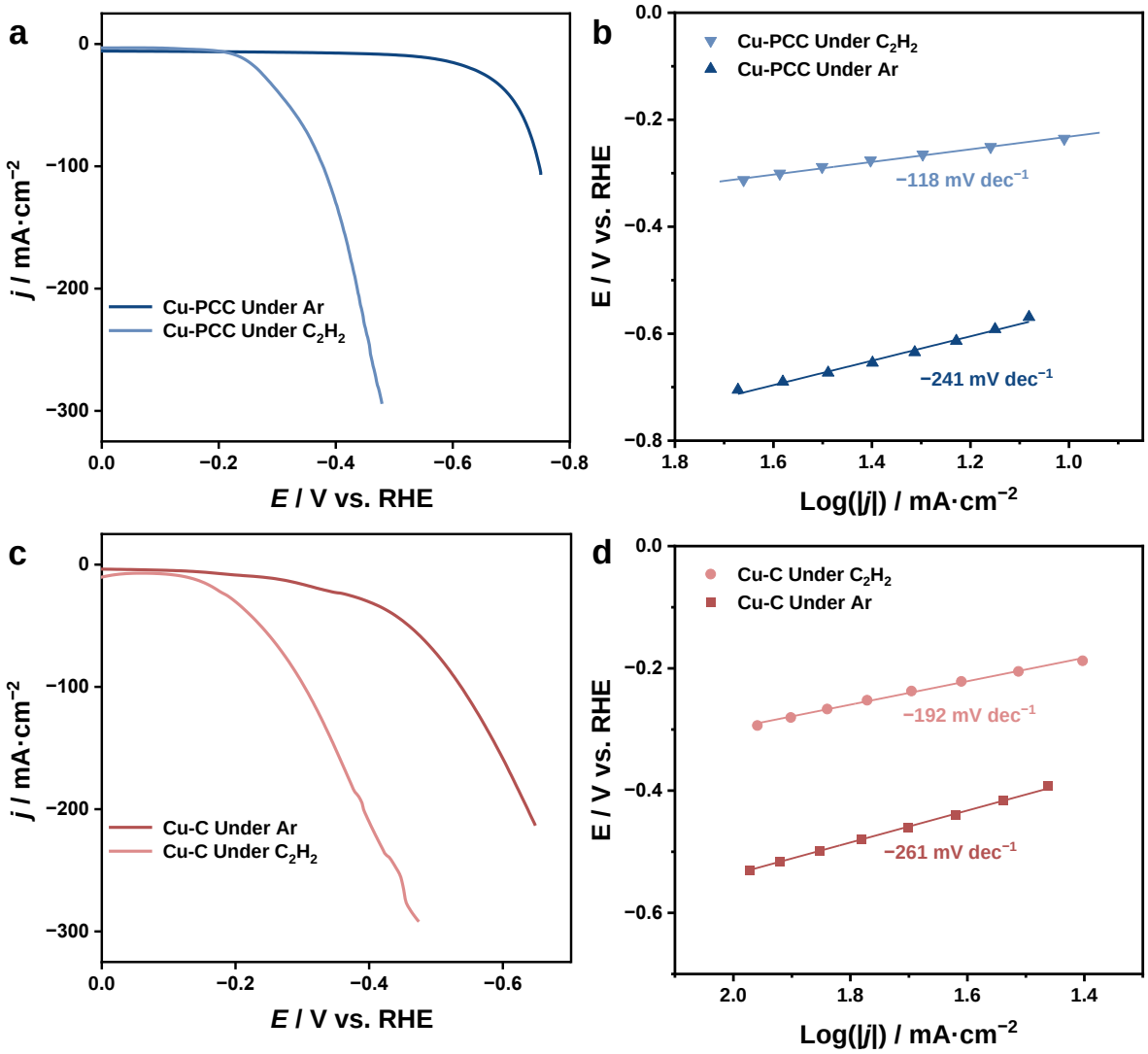

Figure S11. a, b) The LSV curve of Cu-PCC under Ar and C_2H_2 atmospheres (a) and the corresponding Tafel slopes (b); c, d) The LSV curve of Cu-C under Ar and C_2H_2 atmospheres (c) and the corresponding Tafel slopes (d).

Figure S11a, c clearly shows that the onset potential and current density across the whole potential range under a C_2H_2 atmosphere are much greater than those under an Ar atmosphere both over Cu-PCC and Cu-C. In addition, the difference in the absolute value of the Tafel slope of Cu-PCC (241-118=123 mV dec^{-1}) is much greater than that of Cu-C (261-192=69 mV dec^{-1}) (Figure S11b, d), suggesting that the reaction kinetics of C_2H_2 semihydrogenation are enhanced over Cu-PCC due to the enrichment effect caused by the concave surface-induced field.

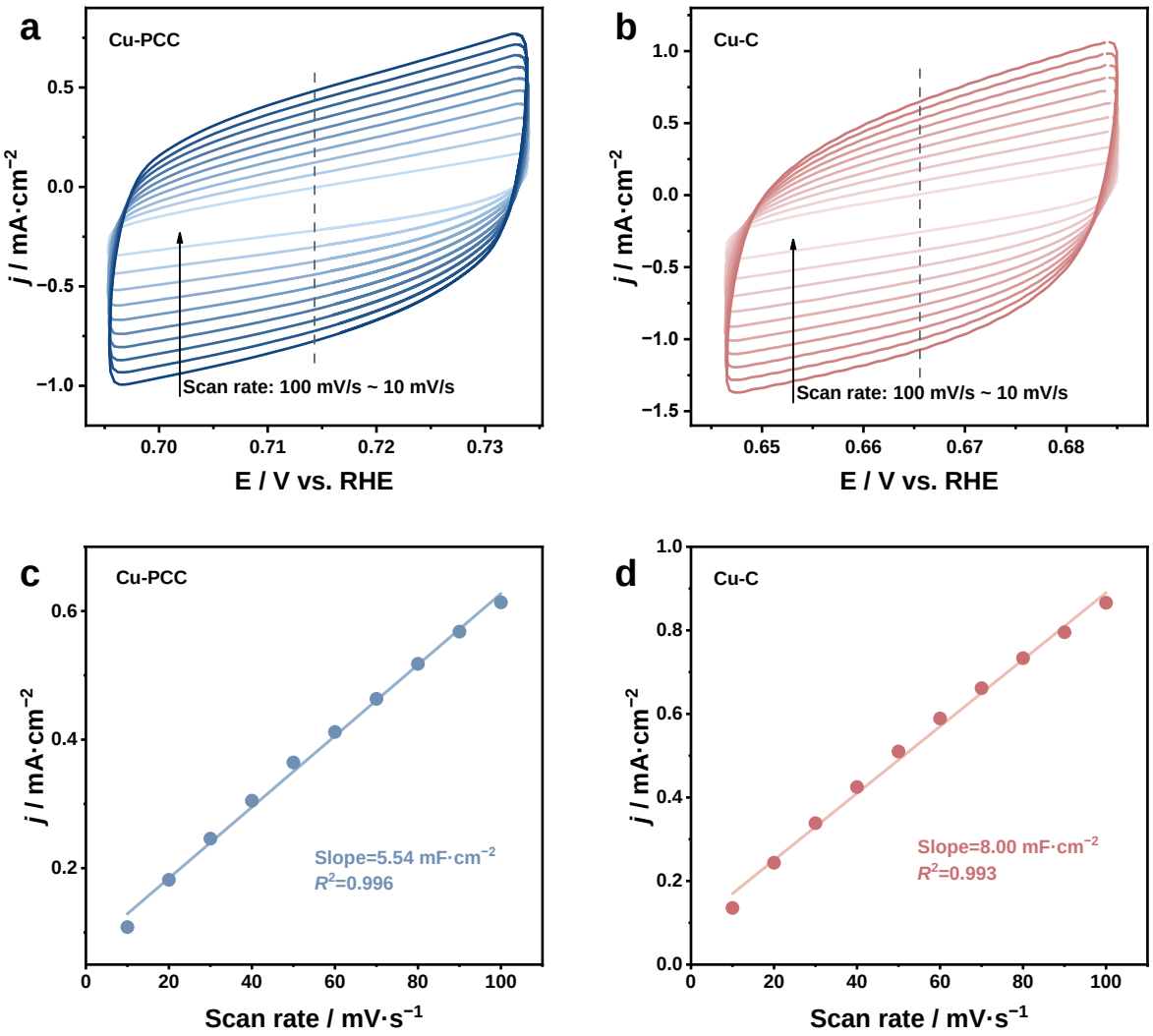

Figure S12. a-d) Electrochemical capacitance measurements. Cyclic voltammogram curves and corresponding fitting of Cu-PCC (a, c) and Cu-C (b, d) with various scan rates.

Electrochemical capacitance measurements were used to determine the ECSA of the catalysts. To measure the electrochemical capacitance, the potential was swept at different scan rates ranging from 10-100 mV/s. The specific capacitance for a flat surface is generally found to be in the range of 20-60 μF cm^{-2}. In the calculations of the ECSA, we assumed a specific capacitance of 40 μF cm^{-2}.

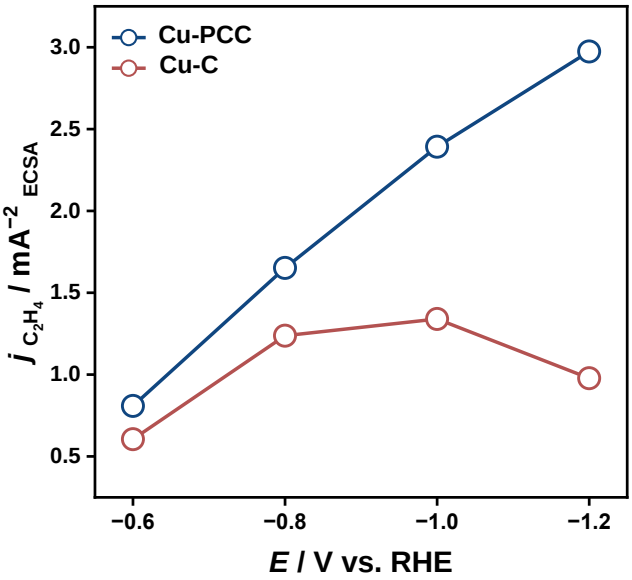

Figure S13. The C_2H_4 partial current densities of Cu-PCC and Cu-C after normalization to the ECSA.

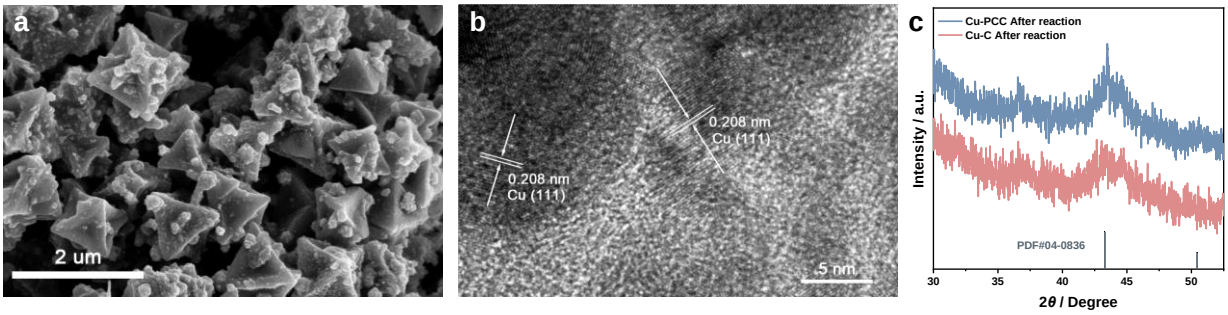

Figure S14. a-c) The stability of the as-prepared ED-Cu NPs. SEM images (a), HRTEM images (b), and XRD patterns (c) after 12 h of continuous testing.

The SEM images after 12 h of continuous testing indicated that the concave surface and particle size of the Cu-PCC could be maintained. The HRTEM images and XRD patterns confirmed that the crystal phase was unchanged, suggesting the robust stability of the as-prepared catalysts.

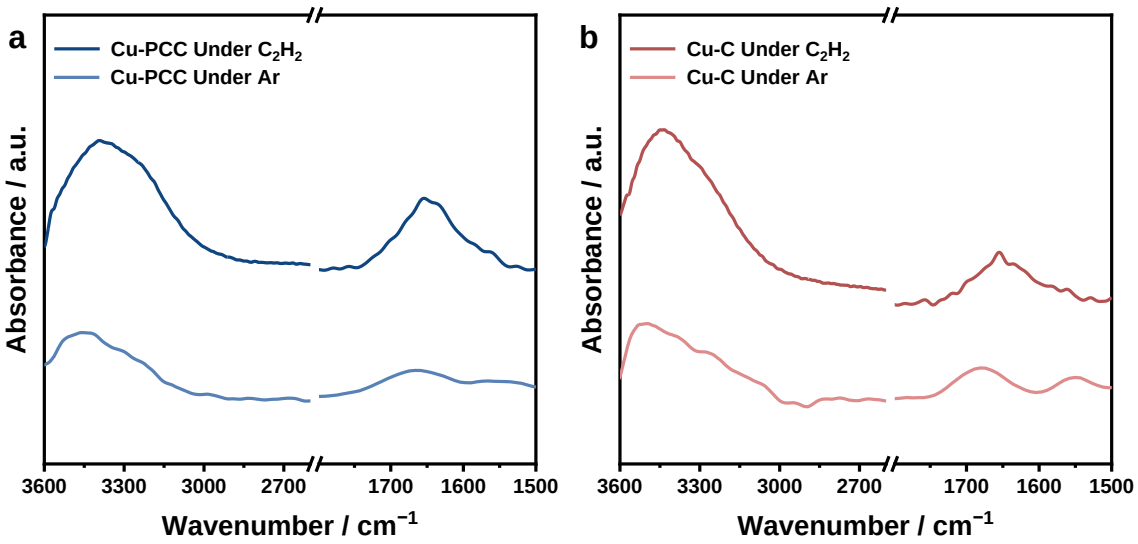

Figure S15. a, b) The ATR-FTIR spectra of Cu-PCC and Cu-C at OCP under Ar and C_2H_2 atmospheres, respectively.

As shown in Figure S15, the peaks located at 3600~3000 cm^{-1} and 1750~1550 cm^{-1} under C_2H_2 are much wider than the corresponding water characteristic peaks under Ar over both Cu-PCC and Cu-C, indicating that the whole peaks under C_2H_2 are attributed to water and C_2H_2. Thus, the relative coverage of water and C_2H_2 could be obtained through peak differentiation and fitting analysis.

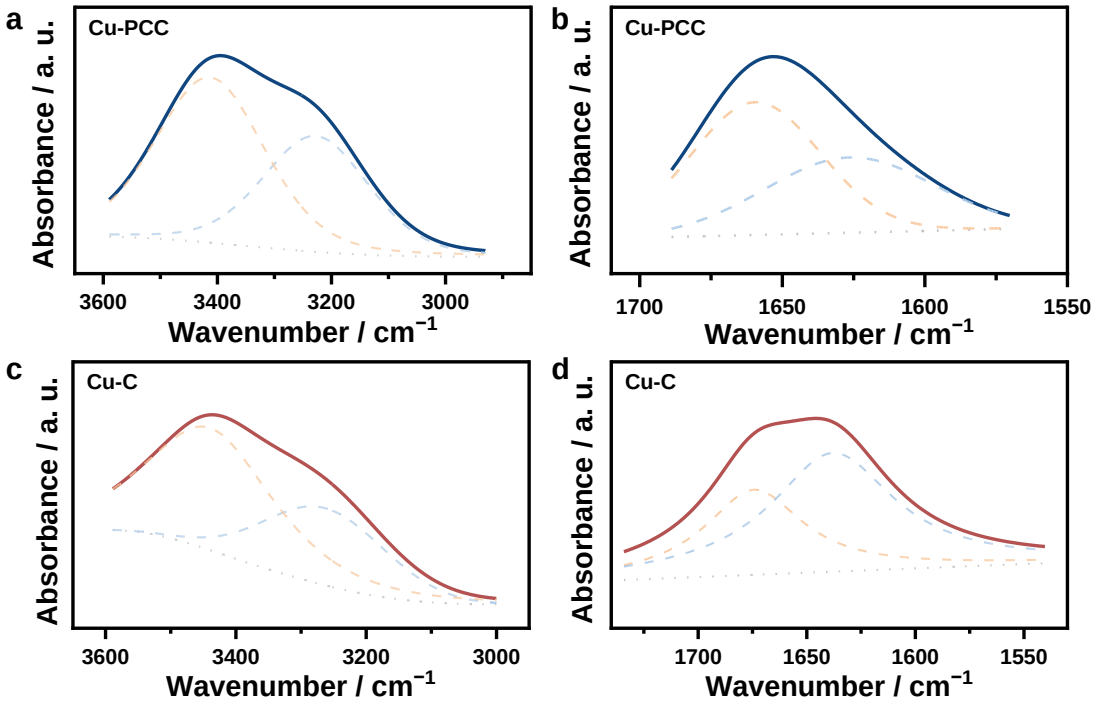

Figure S16. a-d) Peak-differentiating and fitting analysis of the ATR-FTIR data of Cu-PCC and Cu-C under a C_2H_2 atmosphere.

As shown in Figure S16, the peak located at 3600~3000 cm^{-1} at the OCP under a C_2H_2 atmosphere could be divided into two peaks located at ~3410 and ~3200 cm^{-1}, which could be attributed to the *v*(O-H) of water and the *v*(C-H) of C_2H_2, respectively, both over Cu-PCC and Cu-C. In addition, the peak in the range from 1750~1550 cm^{-1} could also be attributed to δ (H-O-H) (~1660 cm^{-1}) and *v*(C≡C) (~1620 cm^{-1}),[11,12], respectively. Note that both the characteristic peaks of *v*(C-H) and *v*(C≡C) exhibit a redshift over Cu-PCC compared to their Cu-C counterparts, indicating that the carbon–carbon bonding of C_2H_2 over Cu-PCC has been weakened due to the delocalization of π electrons.

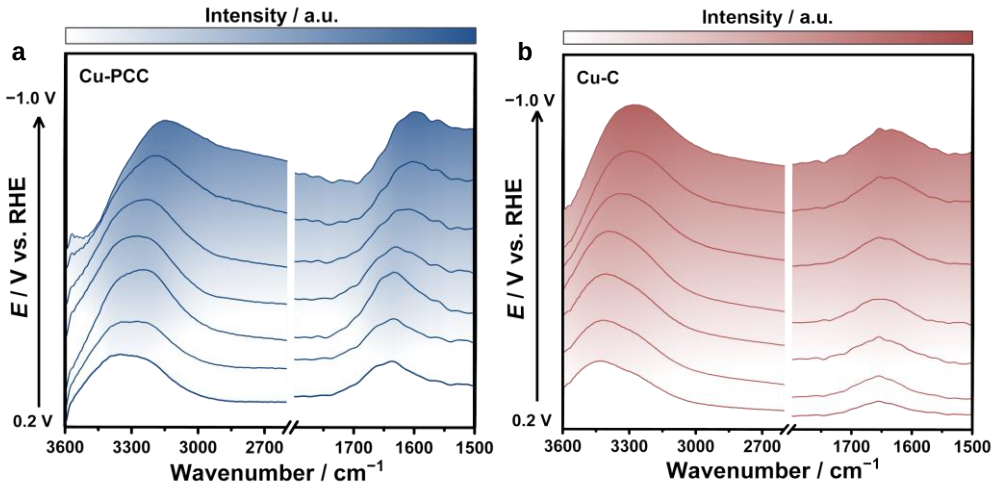

Figure S17. a, b) Potential-dependent *in situ* ATR-FTIR results under a C_2H_2 atmosphere over Cu-PCC and Cu-C.

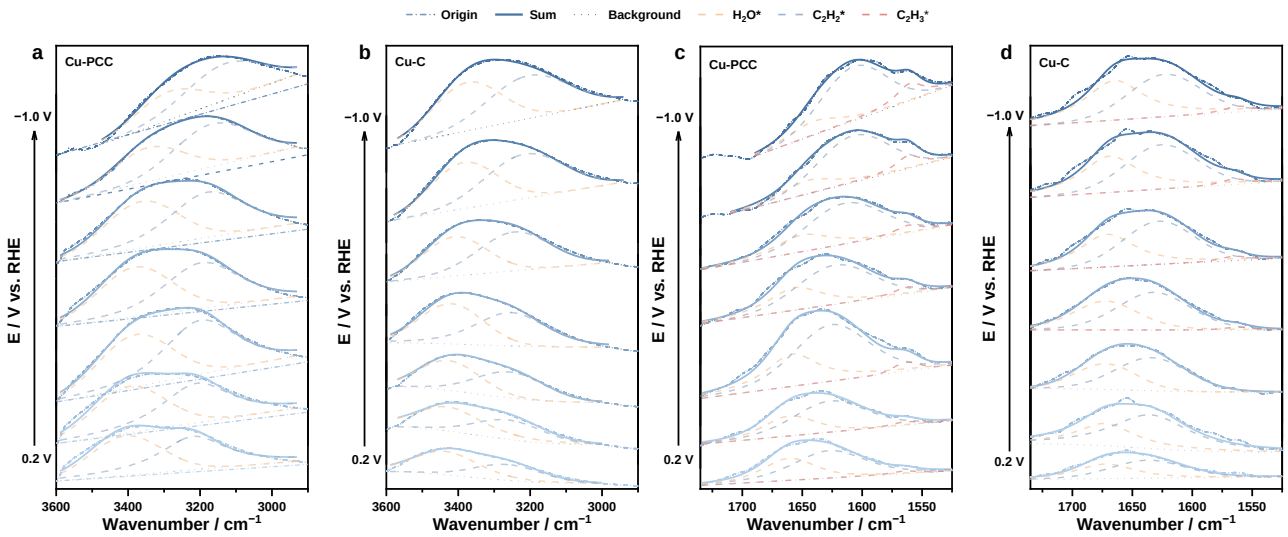

Figure S18. a-d) Peak-differentiating and fitting analysis of the potential-dependent *in situ* ATR-FTIR data of Cu-PCC and Cu-C under a C_2H_2 atmosphere.

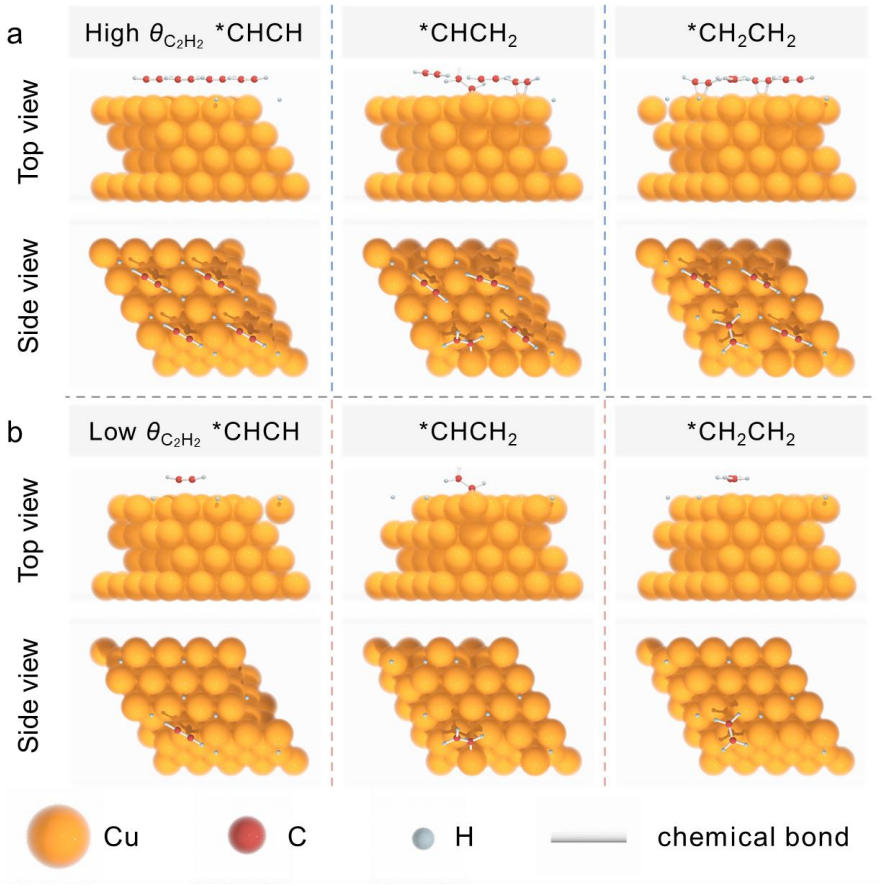

Figure S19. a, b) Theoretical adsorption models of the hydrogenation process of C_2H_2 over high C_2H_2 coverage and low coverage.

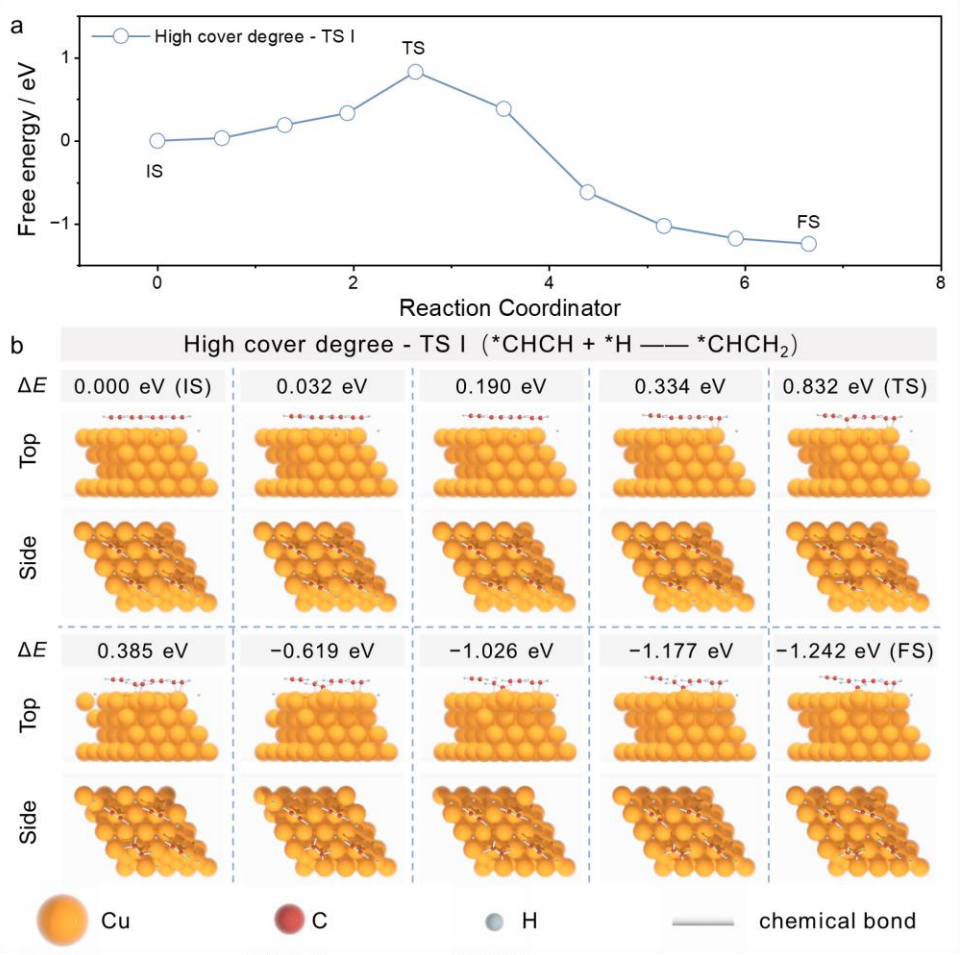

Figure S20. a, b) The energy change profiles and theoretical adsorption models of the transition states for C_2H_2 hydrogenation to C_2H_3 with high C_2H_2 coverage.

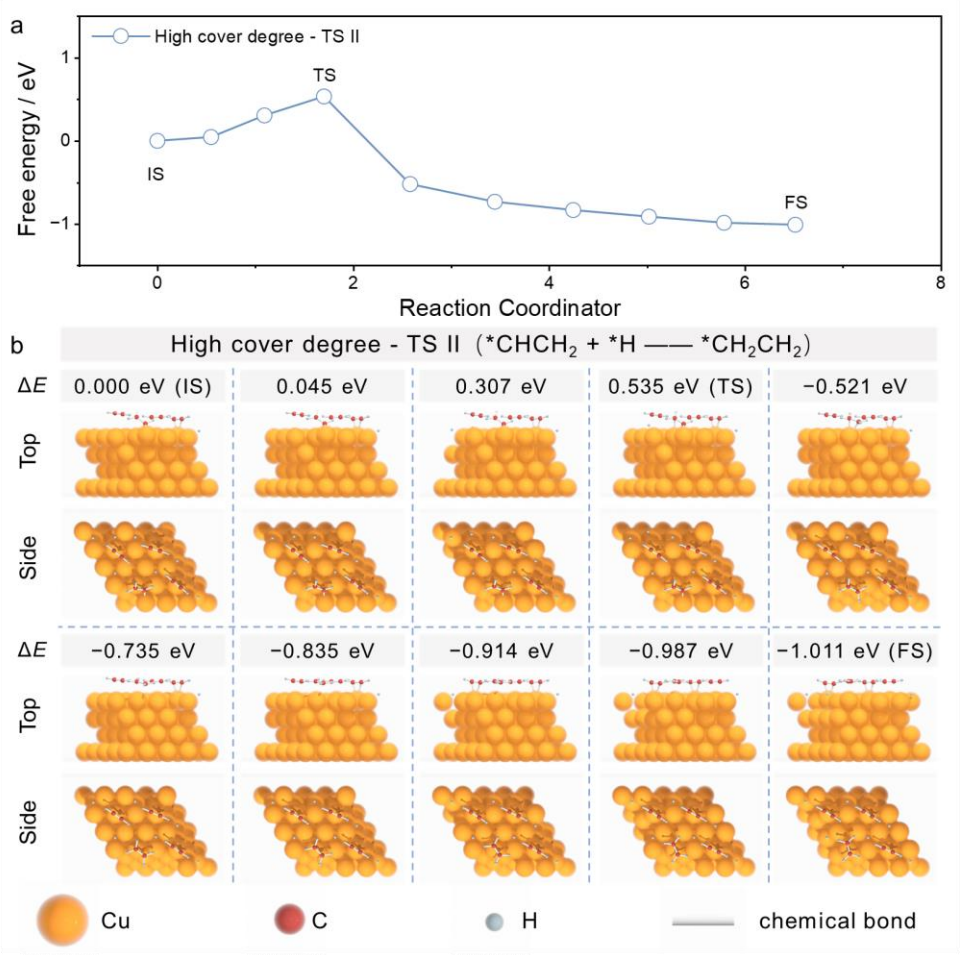

Figure S21. a, b) The energy change profiles and theoretical adsorption models of the transition states for C_2H_3 hydrogenation to C_2H_4 with high C_2H_2 coverage.

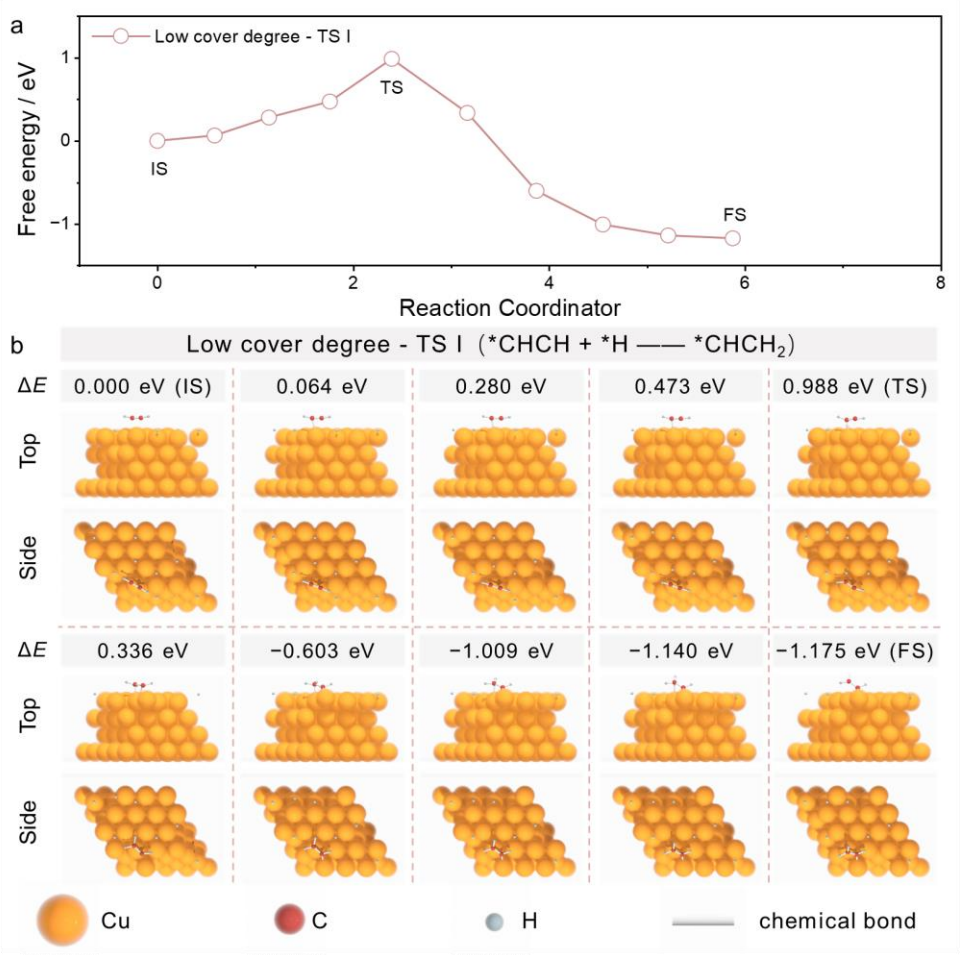

Figure S22. a, b) The energy change profiles and theoretical adsorption models of the transition states for C_2H_2 hydrogenation to C_2H_3 with low C_2H_2 coverage.

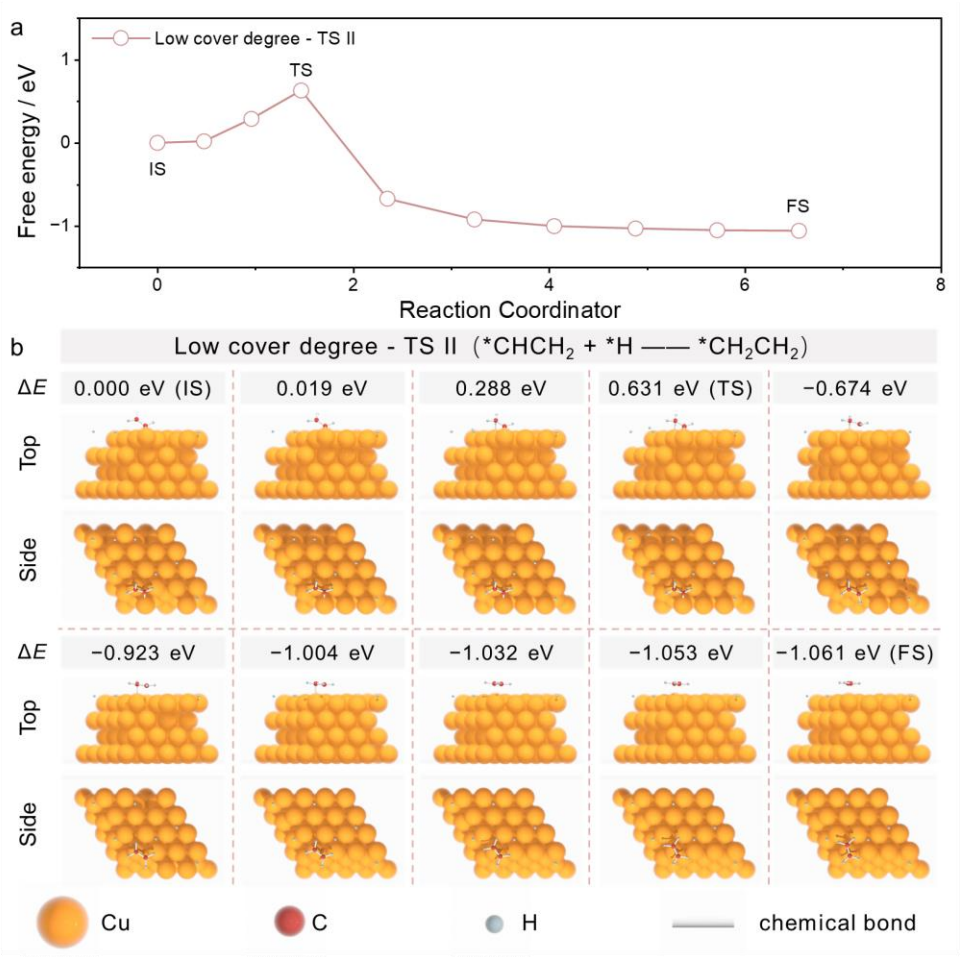

Figure S23. a, b) The energy change profiles and theoretical adsorption models of the transition states for C_2H_3 hydrogenation to C_2H_4 with low C_2H_2 coverage.

References

(1) Chen, S., Wang, C., Zhang, M., Zhang, W., Qi, J., Sun, X., Li, J., N-doped Cu-MOFs for efficient electrochemical determination of dopamine and sulfanilamide. *J. hazard. mater.*, **2020,** *390*, 122157.
(2) G. Kresse, J.Furthmüller, Efficient iterative schemes for ab initio total-energy calculations using a plane-wave basis set. *Phys. Rev. B* **1996**, *54*, 11169.
(3) P. E. Blöchl, Projector augmented-wave method. *Phys. Rev. B* **1994**, *50*, 17953.
(4) J. P. Perdew, K. Burke, M. Ernzerhof, Generalized Gradient Approximation Made Simple. *Phys. Rev. Lett.* **1996**, *77*, 3865.
(5) K. Mathew, R. Sundararaman, K. Letchworth-Weaver, T. A. Arias, and R. G. Hennig, Implicit solvation model for density-functional study of nanocrystal surfaces and reaction pathways *J. Chem. Phys.* **2014**, *140*, 084106.
(6) Guo, L.; Qin, Y.; Jiang, Z.; Jiang, Z.-J., The kirkendall effect-induced formation of FeP@C composites comprising interconnected carbon-coated hollow FeP subnanoparticles for efficient alkaline metal storage. *J. Mater. Chem. A* **2021,** *9* (34), 18231-18238.
(7) Shi, Y.; Ji, Y.; Long, J.; Liang, Y.; Liu, Y.; Yu, Y.; Xiao, J.; Zhang, B., Unveiling hydrocerussite as an electrochemically stable active phase for efficient carbon dioxide electroreduction to formate. *Nat. Commun* **2020,** *11*, 3415.
(8) Shi, Y.; Yu, Y.; Liang, Y.; Du, Y.; Zhang, B., *In situ* electrochemical conversion of an ultrathin tannin nickel iron complex film as an efficient oxygen evolution reaction electrocatalyst. *Angew. Chem., Int. Ed.* **2019,** *58* (12), 3769-3773.
(9) Huang, Y.; Fang, Y.; Lu, X. F.; Luan, D.; Lou, X. W., Co_3O_4 hollow nanoparticles embedded in mesoporous walls of carbon nanoboxes for efficient lithium storage. *Angew. Chem., Int. Ed.* **2020,** *59* (45), 19914-19918.
(10) Shi, Y.; Yu, Y.; Yu, Y.; Huang, Y.; Zhao, B.; Zhang, B., Boosting photoelectrochemical water oxidation activity and stability of Mo-doped $BiVO_4$ through the uniform assembly coating of NiFe–phenolic networks. *ACS Energy Lett.* **2018,** *3* (7), 1648-1654.
(11) Ma, C. Y.; Mu, Z.; Li, J. J.; Jin, Y. G.; Cheng, J.; Lu, G. Q.; Hao, Z. P.; Qiao, S. Z. Mesoporous Co_3O_4 and Au/Co_3O_4 Catalysts for Low-Temperature Oxidation of Trace Ethylene. *J. Am. Chem. Soc.* **2010**, *132*, 2608-2613.
(12) Gu, J.; Jian, M. Z.; Huang, L.; Sun, Z. H.; Li, A.; Pan, Y.; Yang, J. Z.; Wen, W.; Zhou, W.; Lin, Y.; Wang, H. J.; Liu, X. Y.; Wang, L. L.; Shi, X. X.; Huang, X. H.; Cao, L. N.; Chen, S.; Zheng, X. S.; Pan, H. B.; Zhu, J. F.; Wei, S. Q.; Li, W. X.; Lu, J. L. Synergizing Metal-Support Interactions and Spatial Confinement Boosts Dynamics of Atomic Nickel for Hydrogenations. *Nat. Nanotechnol.* **2021**, *16*, 1141-1149.